Research Square

Preprints are preliminary reports that have not undergone peer review.
They should not be considered conclusive, used to inform clinical practice,
or referenced by the media as validated information.

Improvement of Two-Phase Flow Simulation in a Thermosyphon Using a New Saturation Temperature Model

Quang-Hat Cao
University of Ulsan
Shehnaz Akhtar
University of Ulsan
Minseong Choi
University of Ulsan
Kyoungsik Chang
University of Ulsan
Sang-Wook Lee
leesw@ulsan.ac.kr

University of Ulsan

Article

Keywords: Thermosyphon, Heat pipe, Phase change, OpenFOAM, VOF, Heat transfer

Posted Date: November 4th, 2026

DOI: https://doi.org/10.21203/rs.3.rs-11343224/v1

License: This work is licensed under a Creative Commons Attribution 4.0 International License.
Read Full License

Additional Declarations: No competing interests reported.

Improvement of Two-Phase Flow Simulation in a Thermosyphon Using a New Saturation Temperature Model

Quang-Hat Cao[1], Shehnaz Akhtar[1], Minseong Choi[1], Kyoungsik Chang[1], Sang-Wook Lee[1*]

[1]*School of Mechanical Engineering, University of Ulsan, Ulsan 44610, Korea*

** Corresponding author: Tel: +82-52-259-2765, Fax: +82-52-259-1680*

Email address: leesw@ulsan.ac.kr

Abstract: This study presents a mean saturation temperature model for improving the numerical simulation of thermosyphons (wickless heat pipes) using the open-source CFD framework OpenFOAM. Conventional phase change simulations typically assume a constant saturation temperature; however, this assumption is inadequate during transient operation, particularly during startup, when internal pressure and temperature evolve dynamically. The proposed model derives the saturation temperature as a weighted function of the mean temperatures at the evaporator and condenser sections, based on equilibrium conditions of the Lee phase change model. The solver incorporates the Volume of Fluid (VOF) method for interface tracking, the PIMPLE algorithm for pressure-velocity coupling, and conjugate heat transfer between the fluid and solid wall. The model was validated against published experimental data and prior numerical results across multiple heat flux conditions and geometries. The predicted evaporator wall temperatures show improved accuracy over the constant-saturation-temperature approach, with errors below 6% in all cases. The simulations further reveal a relationship between filling ratio and time to steady operation: lower filling ratios require longer steady-state times. Overall, the proposed OpenFOAM-based solver offers a reliable and accessible tool for simulating phase-change heat transfer in thermosyphon systems.

Keyword: Thermosyphon, Heat pipe, Phase change, OpenFOAM, VOF, Heat transfer

I. Introduction

Due to the absence of high flow resistance and low boiling limit within the wick, thermosyphons or gravity heatpipes hold the potential to be implemented in broader working ranges than wicked heat pipes. The thermosyphon differs from a heat pipe only by the exclusion of an internal wick, and sometimes it is called wickless/gravity heat pipe or thermosyphon [1]. Thermosyphons are widely utilized in aerospace thermal management [2], electronic cooling [3], solar energy [4,5], and for heat pumps application [6]. Thermosyphons have been studied experimentally [7,8], lumped model [9], and computational fluid dynamics (CFD) simulation [10,11], among which CFD offers the advantage of accurately capturing internal flow and heat transfer behavior. In recent years, CFD has been increasingly applied to the study of heat pipes, providing researchers with the opportunity to thoroughly investigate internal flow characteristics and heat transfer performance. This method has proven to be both efficient and cost-effective, prompting a growing number of researchers to combine numerical simulations with experimental approaches. Beiginaloo et al. [12] investigated the optimal lengths of the evaporator, adiabatic, and condenser sections of a thermosyphon heat pipe using CFD and DOE. Their results showed that thermal performance improves with a shorter adiabatic zone and higher heat load and filling ratio values, with optimum values of aspect ratio (AR), heat load, and filling ratio being 0.8325, 246 W, and 85%, respectively. This approach effectively bridges the thermal performance gap between lightweight aluminum and conventional copper heat pipes, making it a promising solution for space thermal management applications. Tarokh et al. [13] showed that a vortex generator inserted into the body of a two-phase closed thermosyphon enhances internal flow and promotes thermal boundary layer mixing, improving convective heat transfer. Numerical simulations using the Lee model and Volume of Fluid method show that positioning the vortex generator in the

adiabatic or condenser section yields the greatest reduction in thermal resistance, at 3.5% and 3.3%, respectively, corresponding to higher liquid-vapor mixture flow velocities in those regions. M. Kim et al. [14] reported that while thermal resistance decreases as both the diameter and filling ratio increase, the effective thermal conductivity peaks when the diameter is small. This suggests that the most efficient heat transfer performance occurs at smaller diameters when paired with a higher filling ratio. X. Wang [15] proposed an improved Lee model incorporating superheat consideration, combined with the VOF method, which demonstrates superior prediction of geyser boiling behavior in two-phase closed thermosyphons compared to the original Lee model. Validated against flow visualization experiments, the model accurately captures periodic geyser boiling cycles of 80-100 seconds, including rapid slug bubble growth during expulsion and surface evaporation with natural convection during incubation, providing a more reliable CFD framework for simulating complex phase-change phenomena in thermosyphons.

Studies on the thermal performance of thermosyphons have covered a wide range of factors, such as phase change models, heat pipe diameter, filling ratio, and inner surface conditions. However, in many of these simulations, the saturation temperature used in the phase change model was derived from experimental measurements and held constant throughout the transient process. While assuming a constant saturation temperature is a common simplification in heat pipe modeling, it may not accurately represent the startup behavior. During startup, the internal pressure of the heat pipe gradually increases until a steady state is reached, meaning that the saturation temperature must inherently vary throughout this process. This transient variation in saturation temperature is an important consideration for accurate thermal modeling of thermosyphons. For instance, Li et al. [16] reported that the model-derived saturation temperature and pressure of the thermosyphon over time aligned consistently with the experiments from ambient temperature to

its steady operating value within 120 s. They developed a transient phase change model using a UDF in ANSYS Fluent, where the saturation temperature is expressed as a function of density, and the overall error of wall temperature is less than 10%. Wang et al. [17] accounted for the temperature-pressure in the phase change model in the loop thermosyphon; the study indicated that under high heat flux conditions; loop thermosyphons with elevated filling ratios exhibit superior heat transfer performance compared to those with lower filling ratios.

Heat pipe technology remains an active area of research. Despite this activity, a gap still exists in predicting the saturation temperature for modeling wickless heat pipes (thermosyphons). This study addresses this gap by proposing a mean saturation temperature approach implemented in OpenFOAM. Furthermore, open-source CFD codes such as OpenFOAM currently offer limited capabilities for simulating phase change, particularly for conjugate heat transfer problems involving phase change.

In the present work, a new saturation temperature model is proposed that considers the saturation temperature as a function of the mean temperature of the evaporator and condenser sections of a thermosyphon. Numerical simulations are performed in OpenFOAM, where the Lee phase change model is employed to simulate evaporation, condensation, and conjugate heat transfer processes. The proposed model is validated against available experimental data and previously published numerical results. Furthermore, the effect of filling ratio on steady-state time is also investigated.

II. Method

An evaporating-condensing two-phase flow solver is developed based on the interFoam solver in OpenFOAM (version 8) by incorporating the energy equation and phase-change terms. The volume of fluid (VOF) method is employed to capture the liquid-vapor interface, and the flow

92 is assumed to be laminar, incompressible, and two-dimensional. The phase fractions satisfy the
93 algebraic constraint [18–20]:

$$\alpha_l + \alpha_v = 1 \tag{1}$$

94 The vapor fraction is obtained as:

$$\alpha_v = 1 - \alpha_l \tag{2}$$

95 Accounting for interfacial mass transfer between liquid and vapor phases, the mixture continuity
96 equation is written as [18,20]:

$$\nabla \cdot \mathbf{u} = \dot{m}_{lv}\left(\frac{1}{\rho_v} - \frac{1}{\rho_l}\right) \tag{3}$$

97 The phase transport equation for the liquid phase is [18,20]:

$$\frac{\partial \alpha_l}{\partial t} + \mathbf{u} \cdot \nabla \alpha_l + \nabla \cdot [\alpha_l(1-\alpha_l)\mathbf{u}_r] = -\dot{m}_{lv}[\frac{1}{\rho_l} - \alpha_l(\frac{1}{\rho_l} - \frac{1}{\rho_v})] \tag{4}$$

98 where $\mathbf{u}$ is velocity, $\mathbf{u}_r$ is interface compression velocity and $\dot{m}_{lv}$ is volumetric mass transfer rate.
99 The momentum equation is given as follows [20]:

$$\frac{\partial(\rho \mathbf{u})}{\partial t} + \nabla \cdot (\rho \mathbf{u}\mathbf{u}) = -\nabla p + \nabla \cdot \mu(\nabla \mathbf{u} + \nabla \mathbf{u}^T) + \rho \mathbf{g} + \mathbf{F}_\sigma \tag{5}$$

100 Mixture properties are evaluated as:

$$\rho = \alpha_l \rho_l + (1-\alpha_l)\rho_v \tag{6}$$

$$\mu = \alpha_l \mu_l + (1-\alpha_l)\mu_v \tag{7}$$

$$k = \alpha_l k_l + (1-\alpha_l)k_v \tag{8}$$

101 where $\mathbf{F}_\sigma$ represents the surface tension force. Surface tension is modeled using the Continuum
102 Surface Force formulation [18,19]:

$$\mathbf{F}_\sigma = \sigma\kappa\nabla\alpha_l \tag{9}$$

where curvature is defined as:

$$\kappa = -\nabla \cdot \left(\frac{\nabla\alpha_l}{|\ \nabla\alpha_l\ |}\right) \tag{10}$$

The temperature-based energy equation including latent heat in fluid region is expressed as [18,20]:

$$\frac{\partial(\rho C_p T)}{\partial t} + \nabla \cdot (\rho C_p T\mathbf{u}) = \nabla \cdot (\mathrm{k}\nabla T) + \dot{m}_{lv} L \tag{11}$$

where L is latent heat of vaporization or condensation. The energy equation in the solid region is given as follows [18]:

$$\rho C_p \frac{\partial T}{\partial t} = \lambda\nabla^2 T \tag{12}$$

Where λ is the thermal conductivity of solid.

In conjugate heat transfer, three temperature variables are defined: the fluid phase temperature T_F, the interface temperature at the fluid-solid boundary T_P, and the solid phase temperature T_S. The perpendicular distances from the interface to the adjacent fluid and solid cells are also defined accordingly. Heat flux continuity across the fluid-solid interface is enforced through the application of a Neumann boundary condition [18,21].

$$k_F \frac{\partial T_F}{\partial z_{p,F}} = k_s \frac{\partial T_s}{\partial z_{p,S}} \tag{13}$$

1. Phase change model and mean saturation model

Phase change between liquid and vapor phases is modeled using the Lee evaporation-condensation model. The mass transfer rate is computed as [18,20]:

$$\dot{m}_{lv} = \alpha_l \, r_e \, \rho_l \frac{T - T_{sat}}{T_{sat}} \text{ for } T > T_{sat} \tag{14}$$

$$\dot{m}_{vl} = \alpha_v \, r_c \, \rho_v \frac{T_{sat} - T}{T_{sat}} \text{ for } T_{sat} > T \tag{15}$$

where r_e and r_c are evaporation and condensation coefficient, respectively.

At steady operating, the net rate of evaporation and condensation must be zero, which means equation (14) and (15) must balance.

$$\int \alpha_l \, \rho_l \, r_e \, \frac{T - T_{sat}}{T_{sat}} \, dV_e = \int \alpha_v \, \rho_l \, r_c \, \frac{T_{sat} - T}{T_{sat}} \, dV_c \tag{16}$$

By considering the mean temperature of the condenser and evaporator:

$$r_e \, \rho_l \frac{\bar{T}_e - T_{sat}}{T_{sat}} = r_c \, \rho_v \frac{T_{sat} - \bar{T}_c}{T_{sat}} \tag{17}$$

The saturation temperature model becomes:

$$T_{sat} = \frac{A\bar{T}_e + \bar{T}_c}{\mathrm{A} + 1} \tag{18}$$

where $A = \frac{r_e \, \rho_l}{r_c \, \rho_v}$ is a non-dimensional coefficient.

2. Solver algorithm

The solver algorithm proceeds as follows. Within the fluid domain, the saturation temperature is first computed, followed by the Multi-dimensional Universal Limiter for Explicit Solution

(MULES) [18,22] for alpha equation. The velocity field is then predicted, after which pressure-velocity coupling is resolved using the PIMPLE algorithm, which combines the PISO and SIMPLE approaches to ensure stability under transient conditions. Subsequently, the fluid energy equation is solved to obtain the temperature distribution within the fluid domain, before advancing to the solid domain where the solid energy equation is solved to determine the wall temperature distribution. The simulation was conducted with a Courant number of 0.8 and an adaptive time step. Steady state was determined to be reached when the wall-average temperature fluctuation fell below 5 K. The numerical schemes are shown in Table 1 below:

Table 1. Numerical scheme

Term	Discretization scheme
$\frac{\partial(\rho\mathbf{u})}{\partial t}, \frac{\partial(\rho\mathbf{uT})}{\partial t}$	Euler
$\mathbf{u}\cdot\nabla\alpha_l, \nabla\cdot(\rho C_p T\mathbf{u})$	vanLeer
$\nabla\cdot(\rho\mathbf{uu})$	vanLeerV
$\nabla\cdot[\alpha_l(1-\alpha_l)\mathbf{u}_r]$	linear

3. Computational domain

As depicted in Fig. 1, the computational domain of the thermosyphon is modeled using a 2D axisymmetric approach, in which the heat pipe is longitudinally divided into three distinct operational regions: the evaporator section at the bottom, where heat is absorbed and the working fluid vaporizes; the adiabatic (or transport) section in the middle, which is thermally insulated and allows the vapor to flow upward with negligible heat exchange with the surroundings; and the

condenser section at the top, where heat is rejected to an external sink, causing the vapor to condense back into liquid form, with the condensate returning to the evaporator by gravity, thus completing the passive two-phase circulation cycle. The computational mesh was generated using the blockMesh utility in OpenFOAM, as shown in Figure 2. For Case 1, a grid independence study was conducted by testing several mesh resolutions, and a mesh of 88,000 elements was selected as the optimal configuration, where the result variation was 0.2% when increasing the mesh number from 88,000 to 112,500 elements. For Cases 2 to 4, a mesh of 88,000 elements was adopted following the same criterion, where the wall average temperature changed by less than 0.5%. The details of the boundary conditions and mesh parameters are summarized in Table 2. The thermal properties of the liquid and gas phases in this study were taken from [16,23].

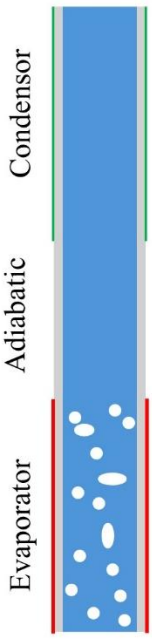


Figure 1. Schematic drawing of thermosyphon

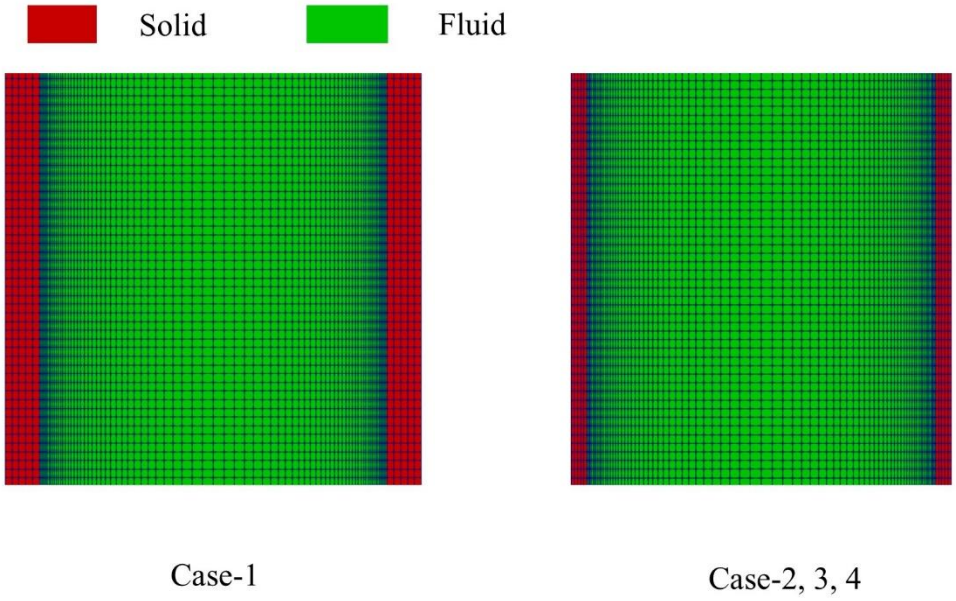


Figure 2. Computational grid

152 **Table 2.** Thermosyphon dimension and boundary condition.

	Case-1	Case-2	Case-3	Case-4
Lengths of sections (cm) (evaporator/adiabatic/condenser)	20/10/20	20/10/20	20/10/20	20/10/20
Outer diameter (mm)	24	22	22	22
Inner diameter (mm)	20	20.2	20.2	20.2
Heat input (W)	600	275.6	299.52	376.14
Convection coefficient ($Wm^{-2}K^{-1}$)	1775.8	824.9	1046.5	1163.5

153

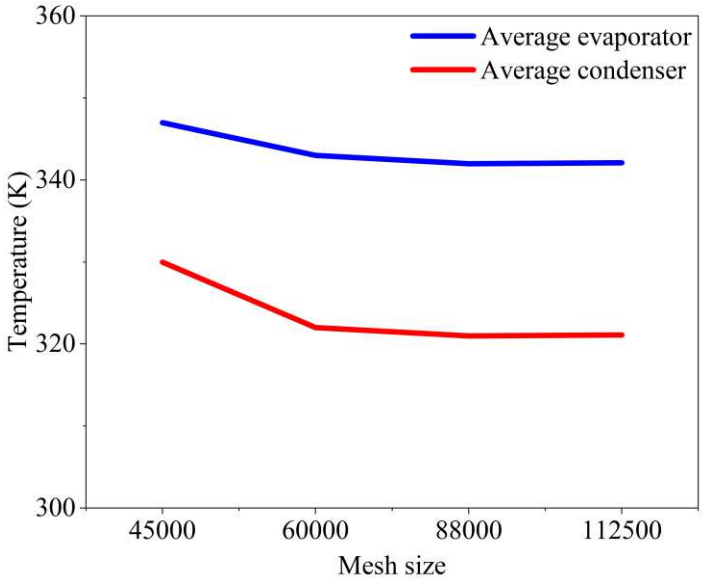


Figure 3(a). Grid independent test for Case-1

154

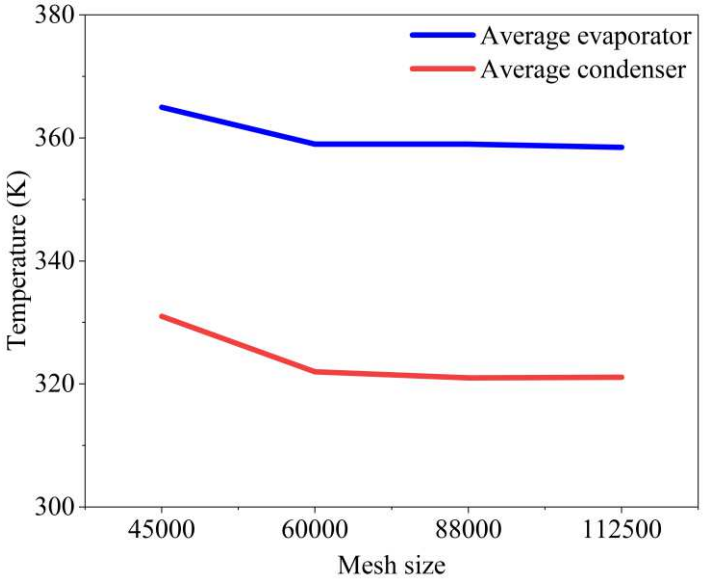


Figure 3(b). Grid independent test for Case-2

III. Results and discussion

1. Validation of numerical simulation in startup of thermosyphon

In order to validate the transient from startup, Case-1 was to verify the present numerical method. The detailed experimental, computational domain, and boundary conditions can be found in [16]. Fig. 4 presents the variation of temperature in different regions of the thermosyphon by comparing the present CFD results with the experimental results from [16]. It can be seen that the temperature profiles in all three sections (evaporator, adiabatic, and condenser) follow trends similar to the experimental measurements, with close agreement in the condenser section, while the evaporator and adiabatic sections show slightly higher values than the experimental data, with a maximum deviation of less than 2%.

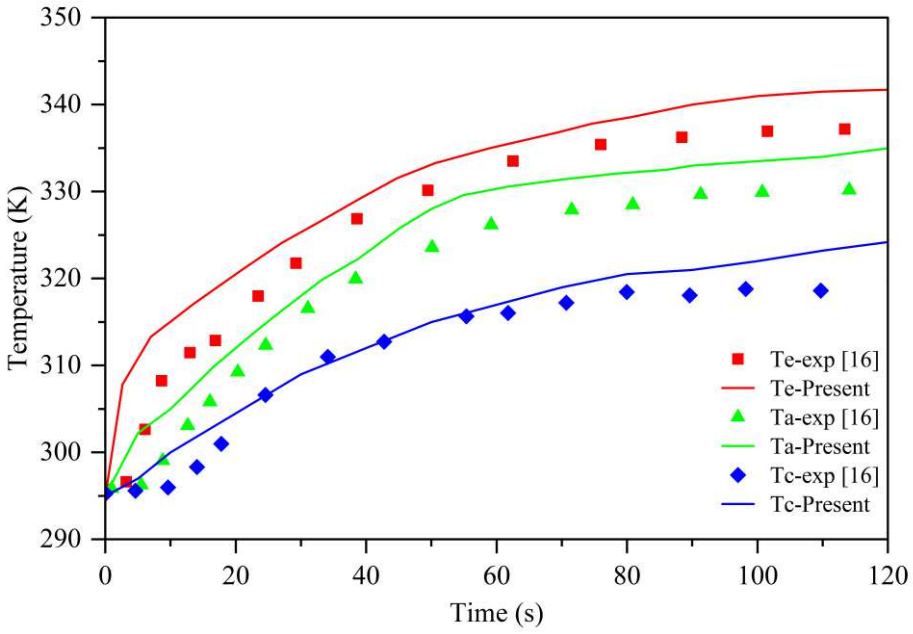


Figure 4. Comparison of temperature in three different sections: evaporator, adiabatic, and condenser

Fig. 5 plots the temperature profile at 120 seconds after the simulation reaches steady state. It can be seen that the new saturation model gives similar trends and values for predicting wall

temperature, especially in the adiabatic section. There is a slight difference in the evaporator section, where the error is 0.6%. Higher deviation can be seen in the condenser section, with the maximum error found at the end of the condenser section, but it is less than 1.8%.

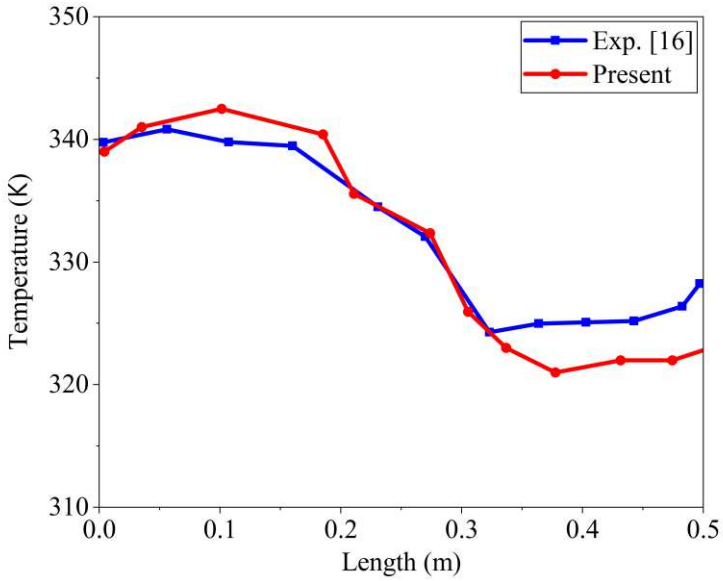


Figure 5. The wall temperature along the axial wall

The process of initial evaporation in the heat pipe is shown in Fig. 6, the evaporator begins at 0-10s and reaches steady state around 120s. In Fig. 6, red and blue colors represent the liquid and vapor phases, respectively. In the evaporator section, the working fluid absorbs heat from the wall and undergoes phase change, forming a pool of vapor bubbles that rise through the liquid toward the adiabatic section; the liquid film is illustrated in Fig. 6. This behavior is consistent with the nucleate boiling characteristic of thermosyphon operation and shows good agreement with the results reported in [16], especially the pool boiling column.

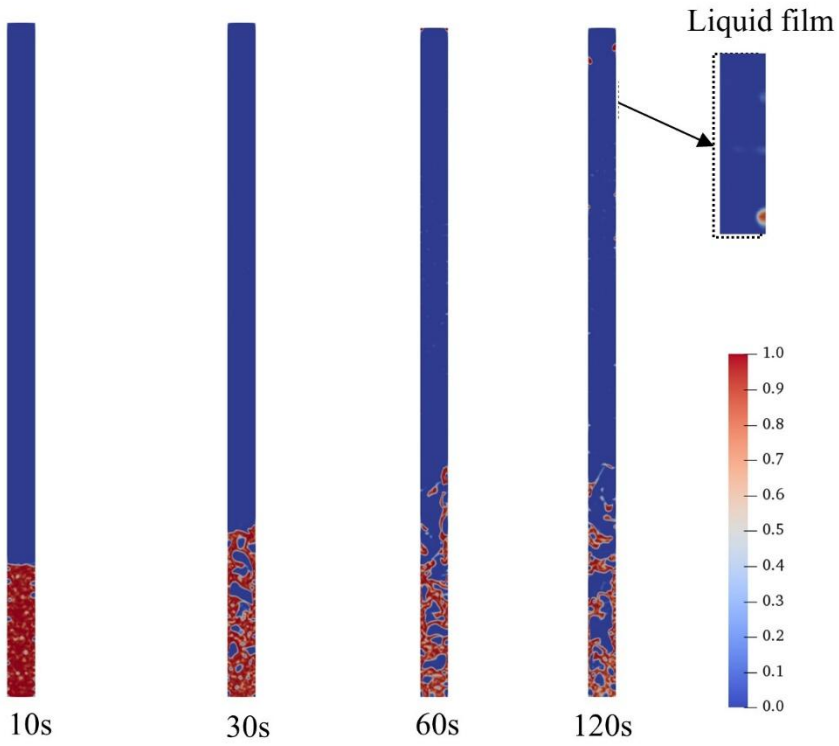


Figure 6. The evolution of volume fraction

2. Comparison of thermal performance at different heat flux

To demonstrate that the proposed method performs reliably independent of geometry and boundary conditions, the following simulations were conducted with various heating power values shown in [23]. The heating power values considered in this study range from 275.6 W to 376.14 W, covering both low and high heating conditions. In the following section, the results of the present study using the mean saturation temperature model are compared in order to assess the improvement in prediction accuracy against those obtained using the constant saturation temperature model reported in [23].

2.1. Thermal analysis

Figure 7 compares the axial wall-temperature distributions obtained experimentally [23], from the constant-saturation-temperature simulation reported in [23], and from the present mean saturation

temperature model at heating powers of 275.6 and 376.14 W. In both cases, the present model reproduces the overall temperature distribution observed experimentally, including the increase in temperature through the evaporator, the relatively stable temperature in the adiabatic section, and the decrease toward the condenser.

The largest deviations for both models occur in the evaporator section, while both approaches converge closely with the experimental data in the condenser, indicating that the evaporator is where the choice of saturation temperature closure matters most. This is physically consistent with the constant-saturation-temperature model's inability to capture the elevated local superheat driving nucleate boiling in the evaporator pool, causing it to systematically overpredict wall temperature there. By weighting T_{sat} toward the evaporator mean temperature (Eq. 18), the present model tracks this locally elevated condition more closely, substantially reducing evaporator-section error relative to the constant model. Notably, the sign of the present model's deviation reverses between the two heat flux cases overprediction at 275.6 W versus underprediction at 376.14 W - suggesting that the coefficient, treated here as constant, may in practice have some dependence on heat flux or boiling regime. This points to spatially- or flux-resolved T_{sat} formulations as a promising direction for further reducing evaporator-section error beyond what a single global mean can achieve.

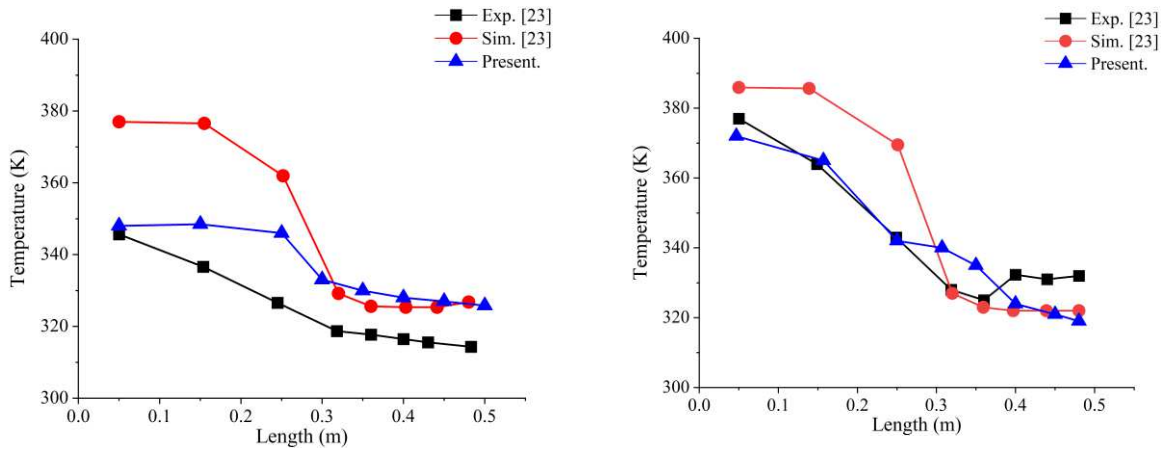


Figure 7. The comparison of wall temperature: Experiment [23], Simulation [23], and the present at 275.6 W (left) and 376.14 W (right)

The performance of thermosyphon can be characterized by the overall thermal resistance. The overall rate of heat transfer to the system is proportional to the effective temperature difference between the heat source to the evaporator and the heat sink from the condenser, and inversely proportional to the equivalent thermal resistance to heat transfer between the two regions. The effective overall thermal resistance can be defined as:

$$R_{CFD} = \frac{T_{e,CFD} - T_{c,CFD}}{Q_{in}} \tag{19}$$

where $T_{e,CFD}$ and $T_{c,CFD}$ are the mean temperature in the evaporator and condenser, respectively. Q_{in} is the heat flux at evaporator.

Fig. 8 compares the predicted thermal resistance against heat flux for the present model, experimental data, and simulation results [23]. All approaches reproduce the same qualitative trend. The present model yields a maximum error of 34%, while the simulation results in [23] show a maximum error of 54.7%. The improvement in thermal resistance can be explained by the improved prediction of evaporator wall temperature, which directly reduces the thermal resistance as shown in Equation (19). While the constant-saturation-temperature approach predicts the

evaporator wall temperature around a fixed saturation value, the present simulation predicts the saturation temperature as a transient quantity that evolves in time.

Overall, the thermal resistance decreases with increasing heating power, which can be attributed to the enhanced evaporation rate at higher heat flux levels, leading to more vigorous vapor generation and improved heat transport within the thermosyphon. This behavior is consistent with the well-known inverse relationship between thermal resistance and heat input reported in the literature [23].

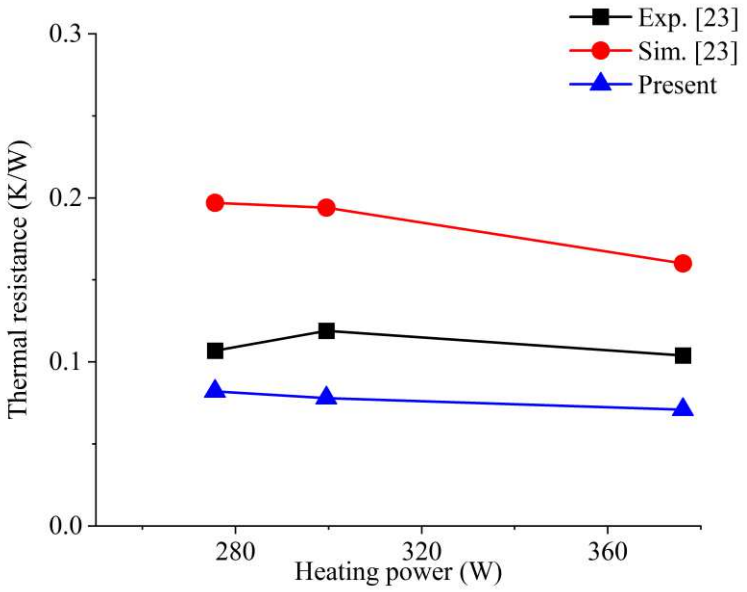


Figure 8. Comparison of thermal resistance at different heat flux power

2.2. Visualization of heat flow behavior

Fig. 9 presents the contours of the volume fraction inside the thermosyphon, for different heating power levels. The red and blue colors are representative of the liquid and vapor phases, respectively. At the evaporator section, heat is supplied, and the liquid receives energy and changes its phase, becoming vapor. The characteristic of this region is a pool of vapor bubbles, indicating active nucleate boiling. At the condenser section, the thermosyphon exchanges heat with the

ambient environment, releasing heat to the surroundings via convection. As a result, the vapor condenses into liquid and falls back to the evaporator pool driven by gravity.

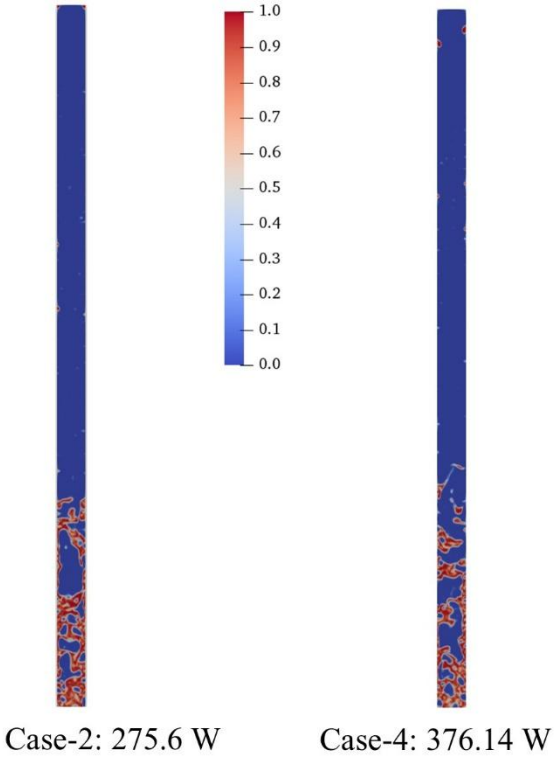


Figure. 9. Comparison of volume fraction at different heat flux power

The temperature contours for different heat flux values are shown in Fig. 10 at t = 35 s, when the thermosyphon has reached steady state. The high-temperature region is located at the evaporator section as a result of the applied heating power. Within this region, the highest temperature occurs at the solid wall and decreases toward the center of the thermosyphon, which is consistent with the radial heat conduction from the heated wall toward the liquid pool. In the condenser section, by contrast, the high-temperature region is located at the center of the thermosyphon due to heat release during phase change, while the temperature is lower near the solid wall owing to convective heat dissipation to the ambient. This opposing radial temperature gradient between the evaporator and condenser sections reflects the distinct heat transfer mechanisms active in each region.

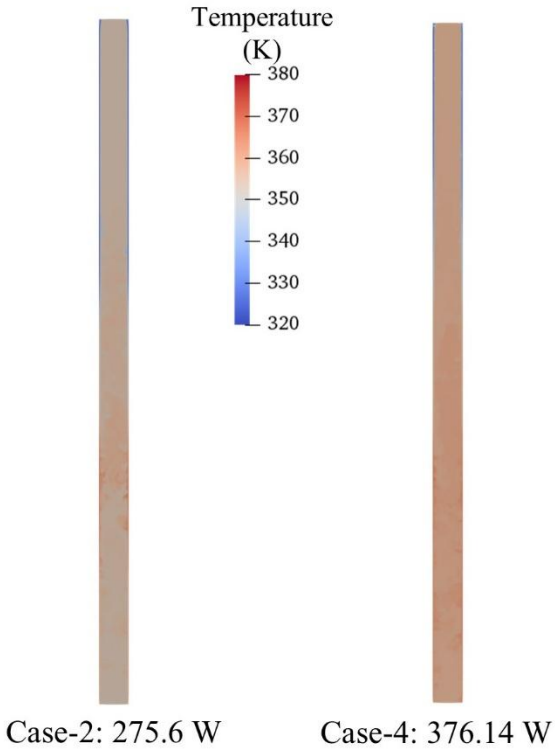


Figure 10. Comparison of the temperature contour at different heat flux powers

3. Effect of filling ratio and steady time

Fig. 11 shows that the steady-state time decreases progressively from 55 s to 18 s as the filling ratio increases from 25% to 100%. At low filling ratios (e.g., 25%), the limited liquid inventory is insufficient to sustain a continuous, stable liquid film or return flow along the heated surface. As a result, the liquid distribution tends to be intermittent, with localized dry patches and re-wetting cycles occurring before a stable flow pattern is established. This intermittent liquid-vapor interaction delays the system from reaching a thermally and hydrodynamically steady state, resulting in a longer steady-state time (55 s). This is corroborated by the steady-state temperature contours in Fig. 12, which show a pronounced high-temperature region concentrated in the lower portion of the tube at 25% filling ratio, with a rough, non-uniform boundary indicative of localized dry-out and intermittent wetting at the evaporator surface.

As the filling ratio increases, a larger liquid inventory becomes available to maintain continuous wetting of the heated surface and a more stable liquid return flow via gravity. This suppresses the intermittent dry-out/re-wetting cycles observed at low filling ratios, allowing the two-phase flow pattern to stabilize more quickly. Consequently, the steady-state time decreases progressively, reaching a minimum of 18 s at 100% filling ratio, where the evaporator is fully flooded and liquid supply is no longer a limiting factor. This is also reflected in Fig. 12, where the temperature field becomes progressively more uniform and cooler with increasing filling ratio, culminating in a nearly isothermal profile (325-330 K) at 100%, consistent with a fully wetted, well-mixed liquid pool.

The slope decreases more steeply between 25% and 50% (55 s to 30 s) than between 75% and 100% (25 s to 18 s), indicates that the stabilizing effect of additional liquid inventory becomes less pronounced at higher filling ratios. This suggests that once a sufficient liquid volume is present to maintain continuous wetting, further increases in filling ratio yield diminishing returns in reducing the steady-state time.

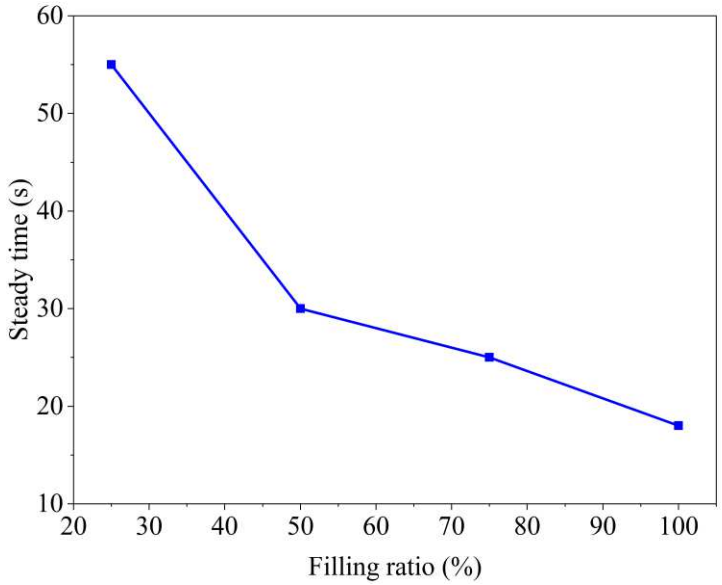


Figure. 11. Comparison of steady time at different filling ratios: Case-2

267

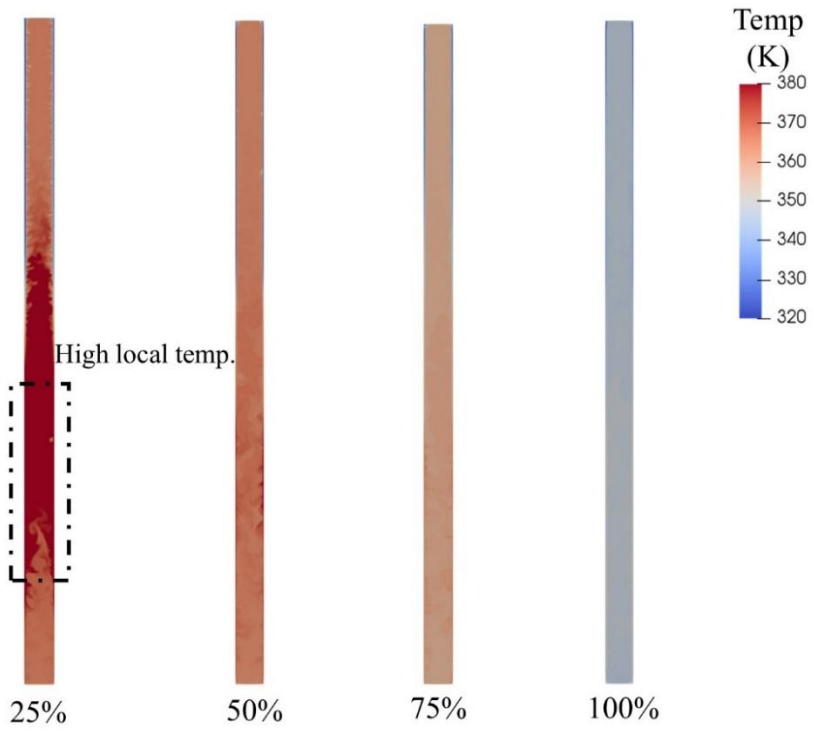


Figure. 12. Comparison of temperature contour with various filling ratios: Case-2

IV. Conclusion

A mean saturation temperature phase change model with conjugate heat transfer was successfully developed using the OpenFOAM computational framework, an open-source CFD code. The proposed solver employs a new saturation temperature formulation capable of predicting both the wall temperature and the saturation temperature inside the thermosyphon. The mean saturation model demonstrates improved prediction of the wall temperature at the evaporator section, which is the most critical region in thermosyphon thermal design. The predicted evaporator wall temperatures show improved accuracy over the constant-saturation-temperature approach, with errors below 6% in all cases. The results also revealed that the steady-state time decreases progressively as the filling ratio increases, dropping by approximately a factor of three as the filling ratio increases from 25% to 100%. These findings demonstrate the potential of the proposed OpenFOAM-based solver as a reliable and accessible tool for the simulation of phase change heat transfer in thermosyphon systems. Several limitations should be noted. The present model assumes a two-dimensional, laminar, incompressible flow, neglects non-condensable gases, which likely contributes to the larger deviations observed in the condenser section. Future work will extend the model to three-dimensional, broader-range, and multi-fluid conditions, and refine the saturation temperature closure to include local phase-fraction and volume weighting.

Acknowledgement

This work was supported by the "Regional Innovation System & Education (RISE)" through the Ulsan RISE Center, funded by the Ministry of Education (MOE) and the Ulsan Metropolitan City, Republic of Korea. (2025-RISE-07-001).

Data Availability

Data will be made available on request

Declaration of competing interest

The authors declare that they have no known competing financial interests or personal relationships that could have appeared to influence the work reported in this paper.

Nomenclature

t	Time, s
u	Velocity, ms^{-1}
u_r	Compression velocity, ms^{-1}
$\dot{m}_{lv}$	volumetric mass transfer rate, $kgm^{-3}s^{-1}$
p	Pressure, Pa
g	Gravity, ms^{-2}
k	Thermal conductivity, $Wm^{-1}K^{-1}$
F	Surface tension force, N
C_p	Specific heat, $Jkg^{-1}K^{-1}$
T	Temperature, K
T_{sat}	Saturation temperature, K
L	Latent Heat, Jkg^{-1}
r_e	Evaporation coefficient, s^{-1}

r_c	Condensation coefficient, s^{-1}

Greek symbols

α	Liquid fraction
ρ	Density, kgm^{-3}
μ	Viscosity, Pas
κ	Curvature, m^{-1}
σ	Surface tension Nm^{-1}
λ	Solid thermal conductivity, $Wm^{-1}K^{-1}$

References

[1] H. Shabgard, M.J. Allen, N. Sharifi, S.P. Benn, A. Faghri, T.L. Bergman, Heat pipe heat exchangers and heat sinks: Opportunities, challenges, applications, analysis, and state of the art, Int. J. Heat Mass Transf. 89 (2015) 138–158. https://doi.org/10.1016/j.ijheatmasstransfer.2015.05.020.

[2] Y. Cao, M. Gao, Wickless network heat pipes for high heat flux spreading applications, Int. J. Heat Mass Transf. 45 (2002) 2539–2547. https://doi.org/https://doi.org/10.1016/S0017-9310(01)00338-6.

[3] S. Tundee, N. Srihajong, S. Charmongkolpradit, Electric power generation from solar pond using combination of thermosyphon and thermoelectric modules, Energy Procedia 48 (2014) 453–463. https://doi.org/10.1016/j.egypro.2014.02.054.

[4] L. Chen, X.-R. Zhang, Experimental analysis on a novel solar collector system achieved by supercritical CO2 natural convection, Energy Convers. Manag. 77 (2014) 173–182. https://doi.org/https://doi.org/10.1016/j.enconman.2013.08.059.

[5] L. Zhang, L. Fan, M. Hua, Z. Zhu, Y. Wu, Z. Yu, Y. Hu, J. Fan, K. Cen, An indoor experimental investigation of the thermal performance of a TPLT-based natural circulation steam generator as applied to PTC systems, Appl. Therm. Eng. 62 (2014) 330–340. https://doi.org/https://doi.org/10.1016/j.applthermaleng.2013.09.045.

[6] P. Byrne, J. Miriel, Y. Lenat, Experimental study of an air-source heat pump for simultaneous heating and cooling – Part 2: Dynamic behaviour and two-phase thermosiphon defrosting technique, Appl. Energy 88 (2011) 3072–3078. https://doi.org/https://doi.org/10.1016/j.apenergy.2011.03.002.

[7] Y. Naresh, C. Balaji, Experimental investigations of heat transfer from an internally finned two phase closed thermosyphon, Appl. Therm. Eng. 112 (2017) 1658–1666. https://doi.org/10.1016/j.applthermaleng.2016.10.084.

[8] A. Brusly Solomon, A. Mathew, K. Ramachandran, B.C. Pillai, V.K. Karthikeyan, Thermal performance of anodized two phase closed thermosyphon (TPCT), Exp. Therm. Fluid Sci. 48 (2013) 49–57. https://doi.org/10.1016/j.expthermflusci.2013.02.007.

[9] H. Shabgard, T.L. Bergman, N. Sharifi, A. Faghri, High temperature latent heat thermal energy storage using heat pipes, Int. J. Heat Mass Transf. 53 (2010) 2979–2988. https://doi.org/10.1016/j.ijheatmasstransfer.2010.03.035.

[10] W. Min, W. Zhong, L. Wang, X. Cao, Y. Yuan, Numerical investigation of the thermal performance of a loop thermosyphon considering dynamic condensation mass transfer time relaxation parameter, Int. J. Heat Mass Transf. 235 (2024). https://doi.org/10.1016/j.ijheatmasstransfer.2024.126210.

[11] A. Alizadehdakhel, M. Rahimi, A.A. Alsairafi, CFD modeling of flow and heat transfer in a thermosyphon, International Communications in Heat and Mass Transfer 37 (2010) 312–318. https://doi.org/10.1016/j.icheatmasstransfer.2009.09.002.

[12] G. Beiginaloo, A. Mohebbi, M.M. Afsahi, Combination of CFD and DOE for optimization of thermosyphon heat pipe, Heat and Mass Transfer/Waerme- Und Stoffuebertragung 58 (2022) 561–574. https://doi.org/10.1007/s00231-021-03130-w.

[13] A. Tarokh, C. Bliss, A. Hemmati, Performance enhancement of a two-phase closed thermosyphon with a vortex generator, Appl. Therm. Eng. 182 (2021) 116092. https://doi.org/10.1016/j.applthermaleng.2020.116092.

[14] M. Kim, J.H. Moon, Numerical investigation and modeling of thermal resistance and effective thermal conductivity for two-phase thermosyphon, Case Studies in Thermal Engineering 27 (2021). https://doi.org/10.1016/j.csite.2021.101358.

[15] X. Wang, Y. Wang, H. Chen, Y. Zhu, A combined CFD/visualization investigation of heat transfer behaviors during geyser boiling in two-phase closed thermosyphon, Int. J. Heat Mass Transf. 121 (2018) 703–714. https://doi.org/10.1016/j.ijheatmasstransfer.2018.01.005.

[16] G. Li, Y. Zhang, G. Zhang, S. Huang, S. Ding, Transient experimental and numerical study of thermosyphon under different heating fluxes and filling ratios, Appl. Therm. Eng. 243 (2024). https://doi.org/10.1016/j.applthermaleng.2024.122514.

[17] K. Wang, C. Hu, B. Jiang, X. Hu, D. Tang, Numerical simulation on the heat transfer characteristics of two-phase loop thermosyphon with high filling ratios, Int. J. Heat Mass Transf. 184 (2022) 122311. https://doi.org/https://doi.org/10.1016/j.ijheatmasstransfer.2021.122311.

[18] Q.H. Cao, S. Akhtar, K. Chang, S.W. Lee, Development and validation of a conjugate heat transfer model with phase change for subcooled boiling flow, J. Vis. (Tokyo). (2026). https://doi.org/10.1007/s12650-026-01142-4.

[19] X. Shi, K. Zheng, B. Yin, Numerical method for gas-liquid two-phase flow with phase change heat transfer considering compressibility using OpenFOAM, International Journal of Thermal Sciences 188 (2023) 108195. https://doi.org/10.1016/j.ijthermalsci.2023.108195.

[20] N. Samkhaniani, M.R. Ansari, Numerical simulation of bubble condensation using CF-VOF, Progress in Nuclear Energy 89 (2016) 120–131. https://doi.org/10.1016/j.pnucene.2016.02.004.

[21] T.L. Perelman, On conjugated problems of heat transfer, Int. J. Heat Mass Transf. 3 (1961) 293–303. https://doi.org/10.1016/0017-9310(61)90044-8.

[22] H.G. Weller, A new approach to VOF-based interface capturing methods for incompressible and compressible flow, OpenCFD Ltd., Report TR/HGW 4 (2008).

[23] B. Fadhl, L.C. Wrobel, H. Jouhara, Numerical modelling of the temperature distribution in a two-phase closed thermosyphon, Appl. Therm. Eng. 60 (2013) 122–131. https://doi.org/10.1016/j.applthermaleng.2013.06.044.